

Ballistic magnon heat conduction and possible Poiseuille flow in the helimagnetic insulator Cu_2OSeO_3

N. Prasai,¹ B. A. Trump,^{2,3} G. G. Marcus,³ A. Akopyan,¹ S. X. Huang,¹ T. M. McQueen,^{2,3,4} and J. L. Cohn^{1,*}

¹*Department of Physics, University of Miami, Coral Gables, FL 33124*

²*Department of Chemistry, Johns Hopkins University, Baltimore, MD 21218*

³*Department of Physics and Astronomy, Institute for Quantum Matter,*

Johns Hopkins University, Baltimore, MD 21218

⁴*Department of Material Science and Engineering,*
Johns Hopkins University, Baltimore, MD 21218

We report on the observation of magnon thermal conductivity $\kappa_m \sim 70$ W/mK near 5 K in the helimagnetic insulator Cu_2OSeO_3 , exceeding that measured in any other ferromagnet by almost two orders of magnitude. Ballistic, boundary-limited transport for both magnons and phonons is established below 1 K, and Poiseuille flow of magnons is proposed to explain a magnon mean-free path substantially exceeding the specimen width for the least defective specimens in the range $2\text{K} < T < 10$ K. These observations establish Cu_2OSeO_3 as a model system for studying long-wavelength magnon dynamics.

I. INTRODUCTION

Spin-mediated heat conduction in ferromagnetic materials has been of interest for decades, but a dearth of suitable ferro- or ferrimagnetic insulators exhibiting magnonic heat conduction has limited investigation [1–8]. The most widely studied example is yttrium-iron garnet (YIG), for which a small magnonic thermal conductivity is well-established at low temperatures. Magnon heat conduction and energy exchange between magnons and phonons have attracted renewed attention recently because of their importance for the burgeoning fields of spin caloritronics [9] and magnon spintronics [10] wherein thermally-driven spin currents induce electrical signals. Essential to the development of related technologies is a deeper understanding of magnon heat conduction and magnon-phonon interactions generally, and identifying suitable materials for realizing practical devices.

Here we report magnon thermal conductivities $\kappa_m \sim 70$ W/mK near 5 K in single crystals of the helimagnetic insulator Cu_2OSeO_3 , far exceeding those observed previously in any other ferro- or ferrimagnets (including YIG). Distinguished in applied magnetic field, both the magnon and phonon (κ_L) thermal conductivities exhibit ballistic behavior below 1 K, with mean-free paths (mfps) limited by the specimen boundaries and $\kappa_m \propto T^2$, $\kappa_L \propto T^3$. At $T > 1$ K, κ_m for clean specimens increases substantially faster than $\propto T^2$ and reaches values twice as large as expected from spin-wave theory. We consider both magnon-phonon drag and Poiseuille flow of magnons as potential mechanisms for this enhancement, and present analysis supporting the latter.

Cu_2OSeO_3 is a cubic material [11, 12] (space group $P2_13$), consisting of a three-dimensional distorted pyrochlore (approximately fcc) lattice of corner-sharing Cu tetrahedra. Inequivalence of the copper sites and strong

magnetic interactions within tetrahedra lead to a 3-up-1-down, spin $S = 1$ magnetic state [13, 14] that persists above the long-range magnetic ordering temperature [15, 16]. Weaker interactions between tetrahedra lead to their ferromagnetic ordering below $T_C \simeq 58$ K. Dzyaloshinsky-Moriya interactions induce a long-wavelength, incommensurate helical spin structure and promote a Skyrmion lattice phase [17, 18] near T_C that has attracted considerable attention. At low temperatures the low-field state is helimagnetic wherein the atomic spins rotate within a plane perpendicular to the helical axis with a wavelength $\lambda_h \simeq 62$ nm; multiple domains with helices aligned along $\langle 100 \rangle$ directions characterize this phase. At $H \gtrsim 300$ Oe the helices of individual domains rotate along the field to form a single-domain, conical phase in which spins rotate on the surface of a cone. Further increasing the field narrows the conical angle until $H \gtrsim 1$ kOe where the ferrimagnetic, collinear-spin state emerges.

II. EXPERIMENTAL METHODS

Phase pure, single crystals of Cu_2OSeO_3 were grown by chemical vapor transport [19]. Cu_2OSeO_3 powder was first synthesized by three stoichiometric (2:1 CuO:SeO₂) heat treatments at 600 °C, each followed by quenching and grinding. The resulting powder was placed in an evacuated fused-silica tube with a temperature gradient of 640 °C - 530 °C, with NH_4Cl as the transport additive. After six weeks, single crystals with typical sizes of 75-125 mm³ were seen, and seed crystals were also added to increase yield. Purity of single crystals were verified by magnetization and X-ray diffraction experiments, showing reproducibility of physical property behavior and good crystallinity.

Specimens were cut from single-crystal ingots, oriented by x-ray diffraction, and polished into thin parallelepipeds. We focus in this work on specimens with heat

* Corresponding Author: cohn@physics.miami.edu

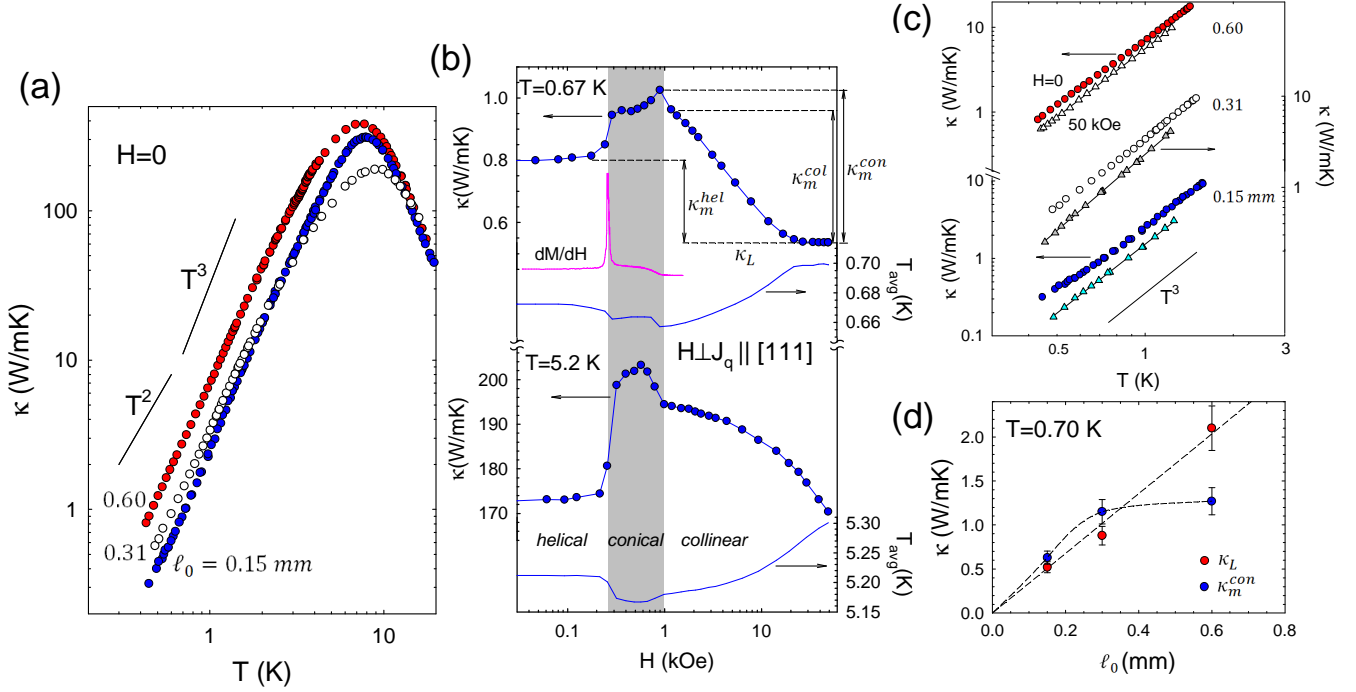


FIG. 1. (a) Thermal conductivity measured along [111] for three specimens (at $H = 0$) labeled by their transverse dimensions ℓ_0 . (b) Magnetic field dependence of thermal conductivity (left ordinates) and average specimen temperature (right ordinates) at two temperatures for $\ell_0 = 0.15$ mm. Also shown in the upper panel is dM/dH at 1.9 K. Here H is the internal field, i.e. corrected for demagnetization. The gray shading delineates the different spin phases. The lattice contribution κ_L is identified as the high-field saturation value of κ for $T = 0.67$ K, and κ_m in the helical, conical, and collinear phases as differences (vertical arrows and dashed lines) (c) Low-T data for the same three specimens from (a) at $H = 0$ (circles) and $H = 50$ kOe (triangles). The solid lines are linear-least-squares fits. (d) κ_L and κ_m^{con} vs. ℓ_0 at $T = 0.70$ K for the three specimens from (a).

flow along the [111] direction and perpendicular magnetic field applied along $[1\bar{1}0]$ for which our data is most extensive. Data for other orientations of heat flow and applied field will be presented elsewhere [20]. A two-thermometer, one-heater method was employed to measure the thermal conductivity in applied magnetic fields up to 50 kOe. Specimens were suspended from a Cu heat sink with silver epoxy and affixed with a 1 k Ω chip heater on the free end. A matched pair of RuO bare-chip sensors, calibrated in separate experiments and mounted on thin Cu plates, were attached to the specimen through 0.125 mm diameter Au-wire thermal links bonded to the Cu plates and specimen with silver epoxy. Measurements were performed in a ^3He “dipper” probe with integrated superconducting solenoid.

A total of 5 different crystals were studied with transverse dimensions, $\ell_0 \equiv 2\sqrt{a/\pi}$ (a is the cross-sectional area) ranging from 0.15-0.60 mm. Three of these ($\ell_0 = 0.15, 0.31, 0.60$ mm) are the primary focus of this work. A fourth crystal for which data is less complete, was cut from the same ingot as $\ell_0 = 0.15$ mm and appears in Fig. 2. Data for the fifth crystal appears in Appendix D, Fig. 7.

III. RESULTS AND DISCUSSION

A. Zero-field thermal conductivity

Figure 1 (a) shows $\kappa(T)$ for $H = 0$ on three crystals labeled by their transverse dimension (ℓ_0). Notable is the magnitude which reaches ~ 400 W/mK (for $\ell_0 = 0.60$ mm) at the maximum near $T = 8$ K, exceptional for a complex oxide. κ is also strongly sample dependent for $T < 10$ K, scaling with ℓ_0 at the lowest T , but not in the region of the maxima. As we discuss further below, the latter feature is attributable to differing point-defect concentrations to which κ_L is sensitive near its maximum. Here we note the likely defects are Se vacancies (common in Se compounds [21]) and numerical modeling of κ_L (Appendices D, E, Fig. 6) implies vacancy concentrations per f.u. of 5.6×10^{-4} , 1.6×10^{-3} , and 4.1×10^{-3} for the specimens with $\ell_0 = 0.15$ mm, 0.60 mm, and 0.31 mm, respectively.

We assume the measured thermal conductivity to be a sum of lattice (phonon) and magnon contributions, $\kappa = \kappa_L + \kappa_m$, valid in the boundary scattering regime ($T \lesssim 3$ K as discussed below) when the phonon-magnon relaxation time (τ_{ph-m}) exceeds, but is comparable to, the phonon-boundary scattering time (τ_b) [22]. Assum-

ing the $q = 0$ relaxation to be representative of the magnon system, an estimate, $\tau_{ph-m} \sim 3 \times 10^{-8}$ s at 30 K, can be inferred from intrinsic ferromagnetic resonance linewidths [23]. Since the magnon density declines as $T^{3/2}$, τ_{ph-m} should increase to $\sim 10^{-7} - 10^{-6}$ s at $T \lesssim 3$ K where $\tau_b = \ell_0/v_{ph} \sim 10^{-7}$ s (using $v_{ph} \approx 2$ km/s); thus the assumption is justified.

B. Ballistic lattice and magnon thermal conductivities distinguished in applied field

The magnetic field dependence of κ through the various spin phases [Fig. 1 (b)], allows for distinguishing κ_L and κ_m . The key features of $\kappa(H)$: (1) abrupt changes of κ at the phase boundaries, (2) a suppression of κ with increasing field in the collinear phase and saturation at the highest fields (50 kOe) and lowest T . Behavior (2) is typical of κ_m in ferro- and ferrimagnets [2–8] – spin-wave excitations are depopulated (gapped) for fields such that $g\mu_B H \gg k_B T$ (Fig. 4 in Appendix A shows that the field at which $\kappa(H)$ saturates corresponds to $g\mu_B H/k_B T \simeq 6$). With [24] $g \simeq 2.1$ the magnon gap is ~ 0.14 K/kOe, such that $\kappa(50 \text{ kOe}) \simeq \kappa_L$ for $T \lesssim 1.2$ K.

We find $\kappa_L \propto T^n$ [triangles, Fig. 1 (c)] with $n = 2.7 - 3$, consistent with phonon mfps limited by the specimen boundaries [Fig. 1 (d)] and nearly diffuse scattering. The Casimir expression for diffuse scattering, boundary-limited thermal conductivity can be used to determine the phonon mean-free path (ℓ_{ph}) [25],

$$\kappa_L = \left(\frac{2\pi^2}{15} \right) \left(\frac{k_B T}{\hbar} \right)^3 k_B \langle v^{-2} \rangle \ell_{ph}$$

where $\langle v^{-2} \rangle = [(1/3)(1/v_{LA}^3 + 2/v_{TA}^3)]^{2/3}$ is the Debye averaged sound velocity. A fit of the low- T $\kappa_L(T)$ data [Fig. 1 (c)] to the form $\kappa_L = AT^n$ yields $A = 1.52, 2.32, 5.62$ and $n = 2.96, 2.80, 2.70$, respectively, for the specimens with $\ell_0 = 0.15, 0.31, 0.60$ mm. The power of T slightly less than 3 is common in insulators [26], indicating some specularity to the boundary scattering. Consistent with observations, the $\ell_0 = 0.60$ mm specimen ($n = 2.70$) was polished on one of its large faces with finer abrasive ($1 \mu\text{m}$) than the other specimens ($5 \mu\text{m}$). Longitudinal and traverse sound velocities for the [111] direction from ultrasonic measurements [27] are $v_{LA} \simeq 3.3$ km/s and $v_{TA} \simeq 1.85$ km/s, respectively. Combining these parameters in the above equation yields $\ell_{ph} \simeq 0.16, 0.24, 0.59$ mm, in good agreement with the effective transverse dimension of the specimens.

The corresponding κ_m in the helical and conical phases computed by subtraction [vertical arrows and dashed lines, Fig. 1 (b)], are $\propto T^2$ for $T \leq 1$ K, consistent with constant magnon mfps (Fig. 2; κ_m^{col} is omitted for clarity). For boundary-limited spin-wave heat conduction we have [1],

$$\kappa_m = \frac{\zeta(3)k_B^3 \ell_m}{4\pi^2 \hbar D} T^2,$$

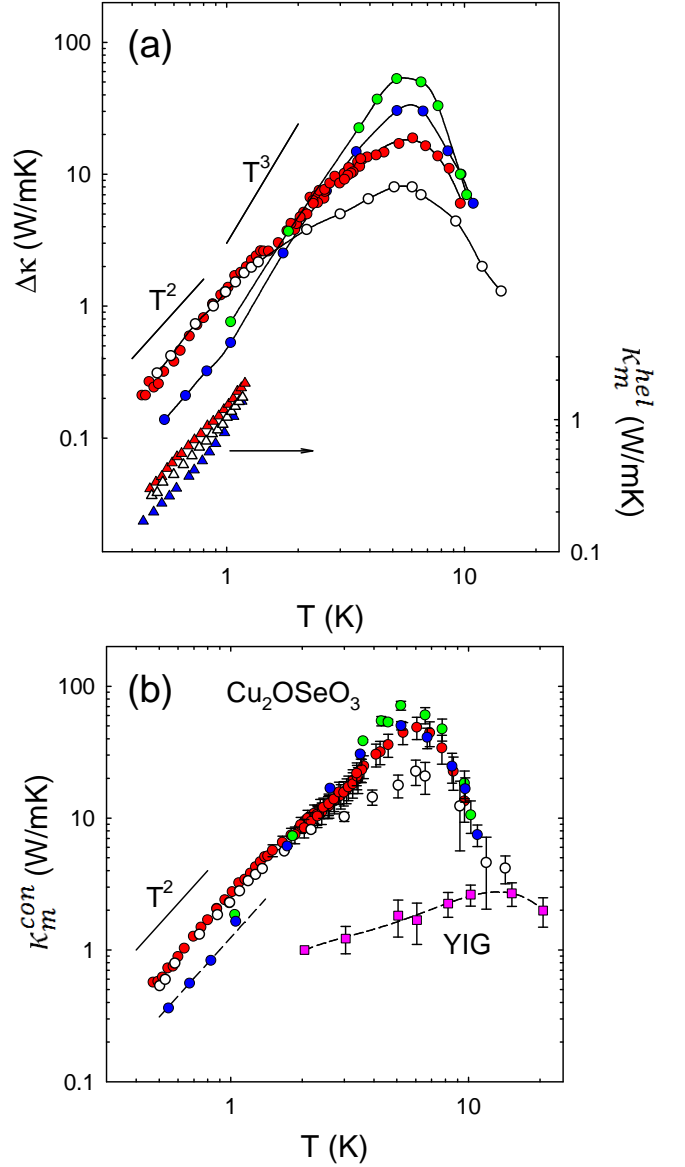


FIG. 2. (a) $\kappa_m^{hel} = \kappa(H = 0) - \kappa(H = 50 \text{ kOe})$ (triangles, right ordinate) and $\Delta\kappa = \kappa_m^{con} - \kappa_m^{hel}$ (circles, left ordinate). (b) κ_m in the conical phase (circles) for the specimens from (a). Error bars reflect uncertainties in the determination of κ_L from the Callaway model (Appendix D, Fig. 6). Also shown are κ_m data for YIG (squares) from Ref. 8.

where $\zeta(3) \simeq 1.202$. A fit of the $\kappa_m^{con}(T)$ data [Fig. 2 (b)] at $T < 1$ K to the form BT^2 gives $B = 1.25, 2.3, 2.6 \text{ W/mK}^3$, respectively, for the specimens with $\ell_0 = 0.15, 0.31, 0.60$ mm; the equation above implies $\ell_m \simeq 0.14, 0.25, 0.28$ mm. The value of ℓ_m for the $\ell_0 = 0.60$ mm specimen is significantly smaller than the specimen dimension, suggesting a maximum magnetic domain size. Similarly, a value of $\ell_m \sim 0.34$ mm for this specimen is inferred from a plot of κ_m vs ℓ_0 [Fig. 1 (d)]. Within the multi-domain helical phase, values for ℓ_m are roughly half as large.

The ballistic character of the magnon transport in the T^2 regime is further corroborated by using kinetic theory to convert κ_m^{con} (or κ_m^{col}) to magnetic specific heat (C_m) and then comparing the latter to expectations of spin-wave theory. We have $C_m = 3\kappa_m/(v_m\ell_m)$, where $v_m = (2/\hbar)Dq$, $D = 52.6$ meV \AA^2 is the spin-wave stiffness [28] (the dispersion at low energy is well-described [29] by $E = Dq^2$). The dominant magnons for boundary-limited κ_m have [30] $q_{dom} = (2.58k_B T/D)^{1/2}$ such that $v_m \simeq 1040T^{1/2}$ m/s. Assuming diffuse scattering of magnons at the crystal (or domain) boundaries, the computed C_m for all crystals agrees well with linear spin-wave theory (Appendix B, Fig. 5).

A transfer of energy from the spin system to the lattice as the magnon gap opens is implied, given the near-adiabatic conditions of the specimens during measurement. The corresponding increase in the average temperature of the sample (T_{avg}) in the high-field regime [solid curves, right ordinates in Fig. 1 (b)] should reflect only a fraction of the total spin energy, since much of it must be distributed within thermometers, thermal links, and heater. As a further self-consistency check on our analysis, this fraction is determined (Appendix C) to be $\sim 4\%$ (30%) at $T = 0.67$ K (5.2 K).

C. Determining the magnon thermal conductivities at higher T

Given that the phonon mfps are boundary-limited at $T \leq 1$ K, the abrupt *increase* in κ at the helical-conical transition [$H \approx 250$ Oe in Fig. 1 (b)] must be attributed to an increase in κ_m associated with the approximate doubling of ℓ_m noted above. It is significant that this jump, $\Delta\kappa = \kappa_m^{con} - \kappa_m^{hel}$ [Fig. 2 (a)], exhibits the same $\propto T^2$ behavior for magnon boundary scattering at low T as found for both κ_m^{hel} and κ_m^{con} computed by subtracting κ_L (Fig. 2). Since $\Delta\kappa$ is independent of any assumptions regarding κ_L , it validates the implicit assumption that κ_L is independent of field.

At $T > 1.2$ K where the applied field is insufficient to fully suppress κ_m , $\Delta\kappa$ represents a *lower bound* on κ_m^{con} [Fig. 2 (b)] since we expect $\kappa_L < \kappa_m^{hel}$ as is clear in the data of Fig. 1 (b) at $T = 5.2$ K. Very similar results for $\Delta\kappa(T)$ were found for a specimen with [110] heat flow and perpendicular field along $[1\bar{1}0]$, thus a large κ_m is not restricted to the [111] direction [20]. The sharp decline of $\Delta\kappa$ at $T \gtrsim 7$ K, and its disappearance for $T \gtrsim 12$ K, indicate that κ_m has a maximum at $T \sim 5 - 6$ K and becomes negligible for $T \gtrsim 12$ K. The latter is supported by recent spin-Seebeck measurements [31] indicating a sharp decline in spin-polarized heat current in the same temperature regime.

To estimate κ_m^{con} at higher T , this behavior of κ_m and the low- T κ_L are exploited as strong constraints on calculations of $\kappa_L(T)$ at $T \geq 1.2$ K using the Callaway model (Appendix D, Fig. 6). This procedure, dictates the error bars on κ_m^{con} in Fig. 2 (b) and, as noted above, provides

estimates of specimen defect (Se vacancy) concentrations (Appendix E).

D. Anomalous T dependence for κ_m and possible Poiseuille flow

A most striking feature of both $\Delta\kappa(T)$ and $\kappa_m^{con}(T)$, aside from unprecedented magnitudes, is their increase, for the two least defective specimens, with a substantially higher power of T than $\propto T^2$ at $T \geq 1$ K (Fig. 2). An additional contribution to C_m from spin-wave "optic" modes cannot be expected in this temperature regime since those sufficiently dispersive to contribute to κ_m have energies exceeding 25 meV [28]. We are aware of only two possible mechanisms that can potentially explain this observation: (1) magnon-phonon drag, (2) Poiseuille flow of magnons. Theory suggests that for momentum-independent magnon relaxation time τ_m , an additive phonon-magnon drag contribution should take the general form [32], $\kappa_{drag} \sim (1/3)C_L v_m^2 \tau_m \propto T^4 \tau_m$, thus offering a stronger T dependence. The relevant magnon-phonon interactions are normal, momentum-conserving processes.

A more intriguing alternative is that magnons undergo Poiseuille flow, predicted 50 years ago for both phonons and magnons [33, 34, 36], but observed only for phonons and only in exceptionally clean materials (e.g. crystalline ^4He [37]). When the mfp for normal scattering (ℓ_N) is much shorter than both the transverse dimension (ℓ_0) and the mfp for bulk resistive scattering processes (ℓ_R), quasiparticles undergo many momentum-conserving scattering events before losing their momentum at the specimen boundaries. Under the stringent conditions $\ell_N < \ell_0/2 < (\ell_N \ell_R)^{1/2}$, the effective mfp approaches that for a particle undergoing random walk with step size ℓ_N , $\text{mfp} \sim \ell_0^2/4\ell_N \gg \ell_0$. We pursue this scenario further since all of the relevant scattering rates for magnons have been computed [35, 36] for a Heisenberg ferromagnet in the low- T regime, and interactions with phonons which underlie phonon-drag are predicted to be significantly weaker.

Forney and Jäckle [36] calculated rates for normal and umklapp magnon scattering and elastic magnon-impurity scattering (non-magnetic defects). The expressions contain three parameters (Appendix F), two of which are set by the lattice constant and exchange coupling. The only remaining free parameter is the defect concentration. Figure 3 (a) shows the relevant mfp's employed for the least defective crystal ($\ell_0 = 0.15$ mm). The conditions for Poiseuille flow are met in the shaded region. κ_m^{con} is computed [solid curves, Fig. 3 (b)] from the kinetic theory expression with a mfp described by an interpolation formula [eq. (F1)] that yields the conventional resistive scattering length well outside the Poiseuille window, $\ell_R^B = (1/\ell_0 + 1/\ell_{3U} + 1/\ell_{4U} + 1/\ell_i)^{-1}$, and tends toward ℓ_0^2/ℓ_N within the Poiseuille regime. Interpolation is controlled by "switching factors" [34, 38] related

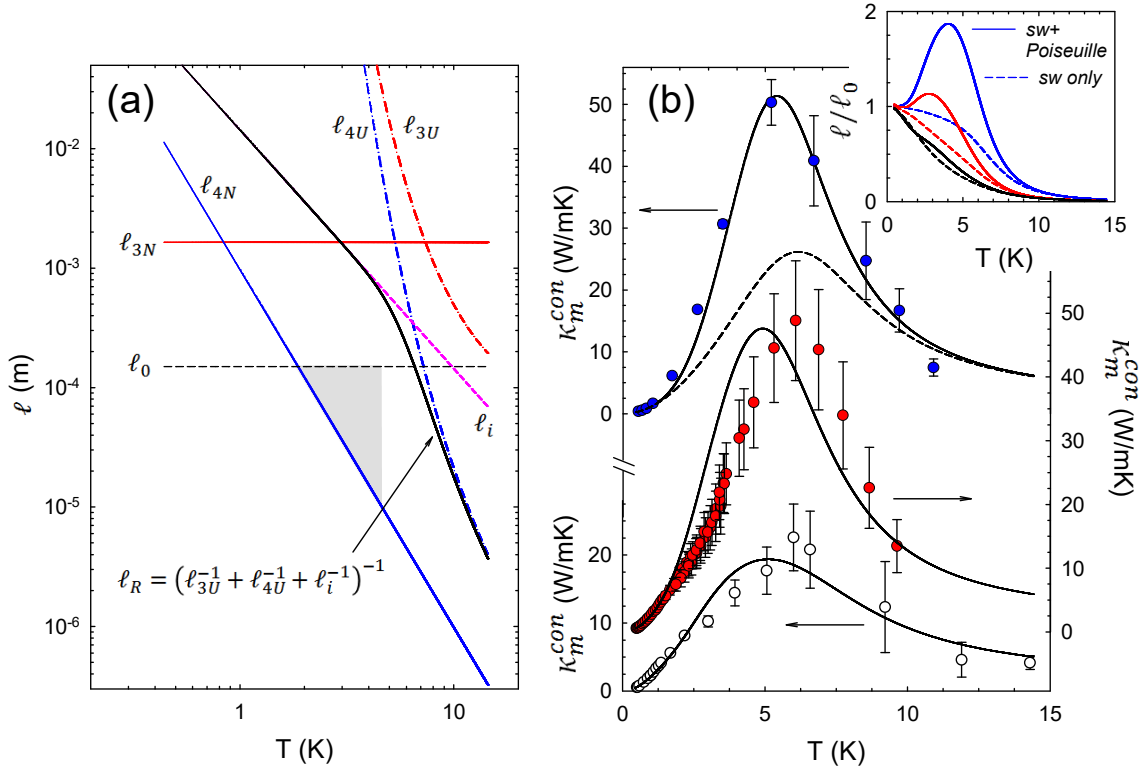


FIG. 3. (a) Magnon mean-free paths for scattering from the model of Ref. 36 (see Appendix F for details). Subscripts refer to 3-magnon and 4-magnon normal (3N, 4N) and umklapp (3U, 4U) processes, elastic impurity scattering (i), and total resistive scattering (R). The Poiseuille conditions (see text) are met in the shaded region. (b) $\kappa_m^{\text{con}}(T)$ for the three crystals from Fig.'s 1 and 2 with linear scaling. The solid curves are model predictions for elastic defect concentrations (from top to bottom in ppm): 12, 22, 62. The dashed curve for the $\ell_0 = 0.15$ mm specimen represents the spin-wave contribution alone without Poiseuille enhancement. Inset: magnon mfps from the model, normalized by low- T boundary-limited values, for each specimen.

to the ratio ℓ_N/ℓ_R (Appendix F and Fig. 8). The data are well-described by the model (with defect concentrations 12, 22, 62 ppm for $\ell_0 = 0.15$ mm, 0.60 mm, and 0.31 mm), though the computed maxima for the more defective specimens deviate from experiment, a consequence of the Poiseuille window being shifted to lower T as the impurity scattering mfp decreases. This may signal inadequacy of the magnon-impurity scattering model, perhaps because spin defects in the present system may be associated with Se vacancies as suggested by a correlation between the defect concentrations inferred for magnons and phonons (Appendix F, Fig.9).

IV. SUMMARY

Our observations reveal Cu_2OSeO_3 to be a model system for further study of long-wavelength magnon dynamics, e.g. our proposal that magnons undergo Poiseuille flow implies that magnon “second sound” might also be observed. Since both the conical and collinear-phase magnon heat conductivities are similar in magnitude, helical magnetism is evidently not the origin of its unusually large κ_m . Since long-wavelength magnons play a

prominent role in the spin-Seebeck effect [8, 9] the results presented here also make it possible to investigate interfacial spin-current transfer using calibrated magnon heat currents and to explore the possible role of the spin phases on transfer efficiency.

V. ACKNOWLEDGMENTS

The authors acknowledge helpful comments from A. L. Chernyshev. This material is based upon work supported by U.S. Department of Energy (DOE), Office of Basic Energy Sciences (BES) Grant No.'s DEFG02-12ER46888 (University of Miami) and DEFG02-08ER46544 (Johns Hopkins University).

Appendix A: Additional low- T $\kappa(H)$ data

Figure 4 shows additional low- T $\kappa(H)$ data showing suppression of the magnon contribution at high fields where we infer $\kappa = \kappa_L$. We also plot the field H_{sat} at which κ becomes field-independent against temperature.

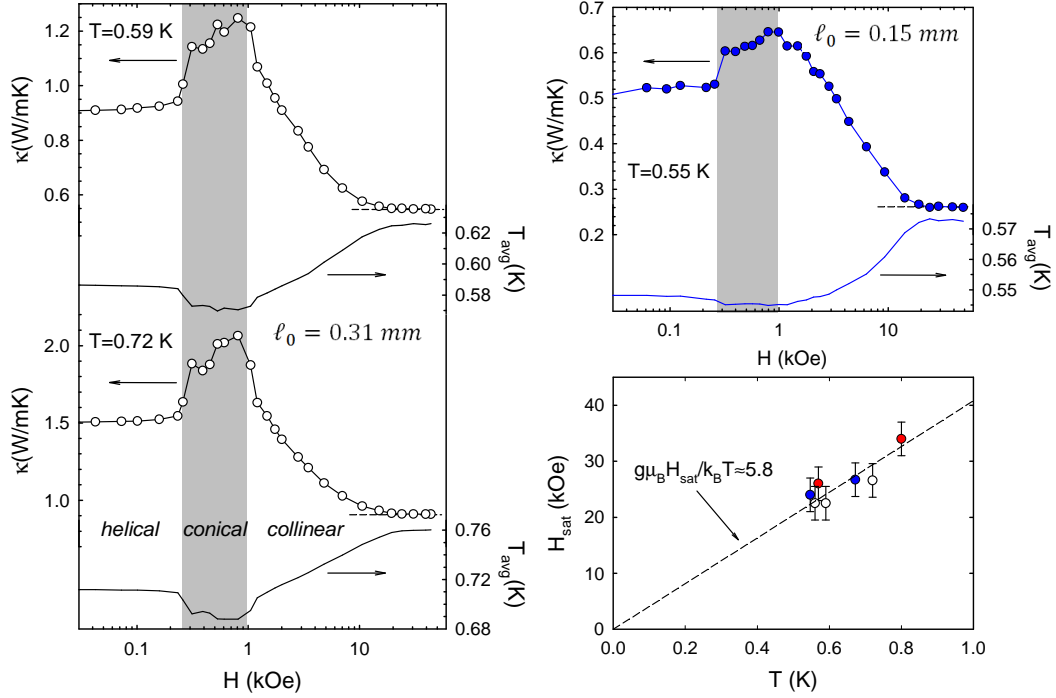


FIG. 4. Magnetic field dependence of thermal conductivity (left ordinates) and average specimen temperature (right ordinates) for $\ell_0 = 0.31$ mm (left panel) and $\ell_0 = 0.15$ mm (upper right panel). The lower right plot shows the field at which κ becomes field-independent, H_{sat} vs. T for all three crystals at the lowest T . Symbols employed are the same as those from Fig.'s 1-3.

Appendix B: Magnetic specific heat computed from

κ_m

As noted in Ref. 28, the Cu_4 tetrahedra of Cu_2OSeO_3 approximate an fcc lattice, the primitive cell of which is 4 times smaller than that of the simple cubic cell. Thus the standard low-temperature form of the magnetic specific heat per volume becomes, $C_m = (0.113/4)k_B (k_B T/D)^{3/2}$ (this factor of 1/4 also appears in expressions for the spin-wave thermal conductivity). Values of C_m (as described in the text) were computed from the measured κ_m^{col} (or κ_m^{con}) using kinetic theory and $\ell_m = \ell_0$ for the four crystals from Fig. 2 (a), with the exception of the $\ell_0 = 0.60$ mm crystal for which we used $\ell_m = 0.34$ mm based on the effective length inferred from Fig. 1 (d). Theory and experiment agree well (Fig. 5).

Appendix C: Energy transfer from spins to lattice at high field

We estimate the fraction of total spin energy transferred to the lattice of the $\ell_0 = 0.15$ mm specimen at $T = 0.67$ K, upon gapping out the spin waves in maximum field [Fig. 1 (b)], as Q/u_m where $Q = C_L \Delta T$ is the heat transferred per volume, computed from the lattice specific heat (C_L) and change in T_{avg} induced by applied field (ΔT), and u_m is the total energy per volume in the spin system,

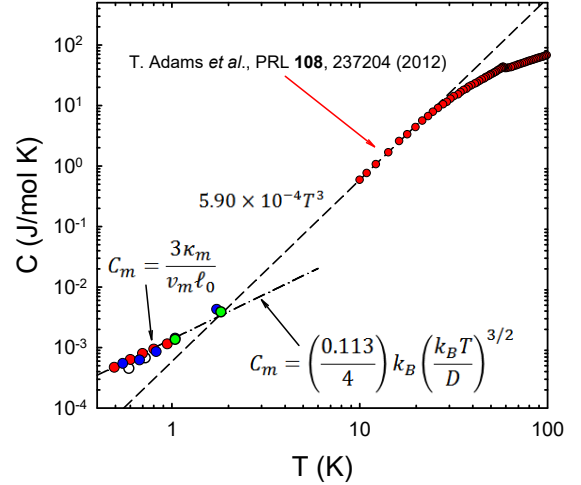


FIG. 5. Measured total specific heat from Ref. 18 and computed magnetic specific heat from kinetic theory using κ_m and effective transverse sample dimension ℓ_0 (specimen symbols are the same as those from Fig.'s 1-3). The dashed line is a T^3 fit to the measured specific heat data at $T < 20$ K, and the dash-dotted line represents the specific heat for an fcc magnetic lattice, converted to molar units for Cu_2OSeO_3 using $1 \text{ mol} = 5.35 \times 10^{-5} \text{ m}^3$.

$$u_m = \frac{D}{16\pi^2} \left(\frac{k_B T}{D} \right)^{5/2} \Gamma(5/2) \zeta(5/2; 1),$$

$\Gamma(5/2) = 3\pi^{1/2}/4$ and $\zeta(5/2; 1) \simeq 1.341$. With $\Delta T = 0.043$ K (Fig. 1b) and using the T^3 fit to the measured specific heat (dashed line, Fig. 5) to compute C_L , we find $Q = 0.14$ J/m³ and $u_m \simeq 3.8$ J/m³, such that $Q/u_m \simeq 0.036$. At $T = 5.2$ K a similar analysis yields $Q/u_m \simeq 0.30$.

Appendix D: Calculations of $\kappa_L(T)$

The Callaway model [39], incorporating its recent update [40], was employed to compute $\kappa_L(T)$ for each of the crystals, with parameter ranges restricted by the following constraints: (1) κ_L fits the low- T , high-field data (where κ_L is inferred directly) and the $T \geq 12$ K, zero-field data (where κ_m is inferred to be negligible by the vanishing of $\Delta\kappa$), (2) the maximum in κ_{con} , computed by subtracting κ_L from κ measured at the conical-collinear transition, should occur at $T \approx 5 - 6$ K where $\Delta\kappa$ has its maximum, (3) $\kappa_L \lesssim \kappa(H = 50\text{kOe})$.

The integral expression for κ_L is,

$$\kappa_L = \frac{k_B}{2\pi^2 v} \left(\frac{k_B}{\hbar} \right)^3 T^3 \left[\int_0^{\Theta_D/T} \frac{x^4 e^x}{(e^x - 1)^2} \tau_C(x, T) dx \right] \left(1 + \frac{\overline{\tau_C(x, T)/\tau_N(x, T)}}{\overline{\tau_C(x, T)/\tau_R(x, T)}} \right),$$

$$\text{with } \overline{f(T)} = \int_0^{\Theta_D/T} \frac{x^4 e^x}{(e^x - 1)^2} f(x, T) dx \Big/ \int_0^{\Theta_D/T} \frac{x^4 e^x}{(e^x - 1)^2} dx,$$

where v is the Debye averaged sound velocity (see above), $\Theta_D = (\hbar v/k_B)(6\pi^2 N/V)^{1/3}$ the Debye temperature, $x = \hbar\omega/k_B T$ the reduced phonon energy, $\tau_C^{-1}(x, T) = \tau_N^{-1}(x, T) + \tau_R^{-1}(x, T)$, and $\tau_N^{-1}(x, T)$ and $\tau_R^{-1}(x, T)$ are phonon scattering rates for normal (momentum conserving) and resistive (momentum non-conserving) processes, respectively. $\tau_R^{-1}(x, T)$ included terms for scattering from boundaries, other phonons (Umklapp scattering), and point-like defects (Rayleigh),

$$\tau_R^{-1}(x, T) = v/\ell_{ph} + Ax^2 T^4 \exp\left(-\frac{\Theta_D}{bT}\right) + Cx^4 T^4,$$

where $\ell_{ph} = \ell_0$ is the boundary-limited phonon mean-free path and A , b , C are constants. The normal scattering rate was taken to have the same frequency dependence as for Umklapp scattering [40], but without the exponential T dependency, $\tau_N^{-1}(x, T) = \gamma Ax^2 T^4$, with γ a

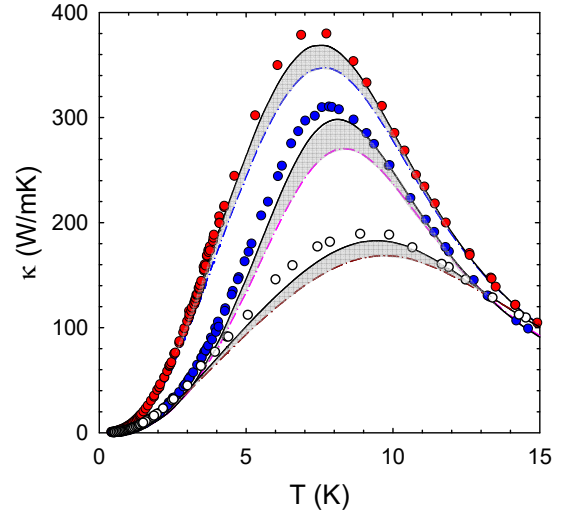


FIG. 6. $\kappa(H = 0, T)$ for the three specimens shown in Fig. 1 (solid circles) and computed κ_L (solid and dash-dotted curves) for two parameter sets for each specimen. Solid curves (from top to bottom, with the same units of Table I): $v = 2.06$, $A = 1.87$, $b = 6.35$, $C = 36$, $\gamma = 1/100$; $v = 2.06$, $A = 1.9$, $b = 6.76$, $C = 10$, $\gamma = 1/50$; $v = 2.35$, $A = 1.72$, $b = 6.35$, $C = 90$, $\gamma = 0$. Dash-dotted curves (from top to bottom): $v = 2.15$, $A = 1.77$, $b = 6.6$, $C = 37$, $\gamma = 1/100$; $v = 2.06$, $A = 1.87$, $b = 6.7$, $C = 14.5$, $\gamma = 0$; $v = 2.35$, $A = 1.5$, $b = 6.35$, $C = 110$, $\gamma = 0$.

constant. A broad range for γ was explored in the fitting and it was found that only for $\gamma \leq 1/50$ were the constraints satisfied. $\gamma = 1/50$ implies a normal scattering rate that begins to exceed that for Umklapp scattering at $T \lesssim 10$ K. Phonon-magnon scattering was assumed to be substantially weaker than other scattering.

Fig. 6 shows $\kappa(H = 0, T)$ data for the three specimens from Fig. 1 along with two κ_L curves for each (solid and dash-dotted curves). These curves border the ranges (shading) defined by the constraints noted above. Data points for κ_m in Fig. 2 (b) correspond to the middle of these ranges with error bars equal to the width of the shaded region. A summary of the scattering parameters is provided in Table I.

In Fig. 7 we compare $\kappa(T)$ at $H = 0$ for the most defective $\ell_0 = 0.31$ mm specimen from Fig.'s 1-3 with a less defective crystal having the same ℓ_0 . Consistent

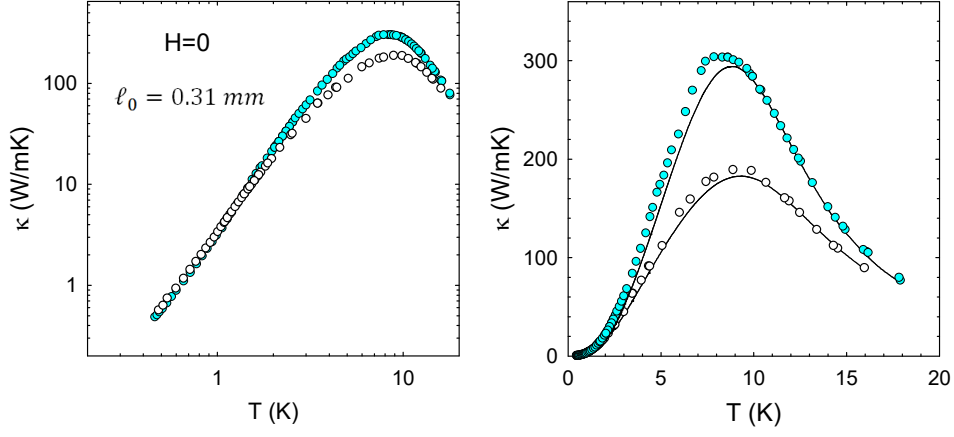


FIG. 7. $\kappa(H = 0, T)$ for two crystals with $\ell_0 \simeq 0.31$ mm in log-log scaling (left) and linear scaling (right). Open circles are for the same crystal from Fig.'s 1-3. Solid curves are produced using the Callaway model using (in units from Table I) $v = 2.35$, $A = 1.72$, $\gamma = 1/50$ and: (upper curve) $b = 6.4$, $C = 26$; (lower curve) $b = 6.2$, $C = 80$.

with expectations, Callaway-model parameter sets for κ_L (solid curves, right panel) differ principally in the defect concentration (C).

Appendix E: Estimate of Se vacancy concentration from point-defect fitting parameters for κ_L

Interpreting the point-defect phonon scattering rate (Table I above) as entirely due to Se vacancies, the vacancy concentration can be estimated using [42],

$$\tau_d^{-1} = \frac{n}{7} \frac{9a^3}{4\pi v^3} \left(\frac{M_{Se}}{\bar{M}} \right)^2 \omega^4,$$

where n is the concentration of vacancies on the Se sublattice, $a = 1.22$ Å is the Se atomic radius, $v = 2060$ m/s is the sound velocity, and $M_{Se}/\bar{M} \simeq 2.05$ is the ratio of the Se mass to the average mass. Using values $C = 13, 37, 95$ K⁻⁴ from Table I for the $\ell_0 = 0.15, 0.60, 0.31$ mm crystals yields concentrations per f.u., 5.6×10^{-4} , 1.6×10^{-3} , 4.1×10^{-3} , respectively.

TABLE I. Ranges of scattering parameters from Callaway modeling of κ_L .

ℓ_0 (mm)	v (km/s)	$A(10^4 \text{ K}^{-4})$	b	$C(\text{K}^{-4})$
0.15	2.06 – 2.15	1.8 – 2.0	6.6 – 6.9	10 – 15
0.31	2.15 – 2.35	1.5 – 1.8	6.0 – 6.6	80 – 110
0.60	2.06 – 2.3	1.75 – 2.0	6.3 – 6.6	34 – 40

Appendix F: Magnon scattering rates and modeling of Poiseuille flow

Forney and Jäckle [36] computed the thermally averaged 3-magnon and 4-magnon normal ($3N$, $4N$) and umklapp ($3U$, $4U$) scattering rates and magnon-impurity scattering rate (i) for a quadratic magnon dispersion within the Born approximation, valid for small impurity concentration, $T \ll T_C$ and $T \gg k_B \Delta$, where Δ is the energy gap (~ 12 μeV for Cu₂OSeO₃):

$$\tau_{3N}^{-1} = 2.6S \frac{k_B}{\hbar} T_d^2 T_e^{-3/2} T^{1/2}, \quad \tau_{4N}^{-1} = 6.1 \times 10^{-4} \frac{k_B T^4}{S^2 \hbar T_e^3},$$

$$\tau_{3U}^{-1} = 1.4 \times 10^3 \frac{S k_B T_d^2}{\hbar (T_e T)^{1/2}} \exp(-12T_e/T), \quad \tau_{4U}^{-1} = \frac{2}{S^2} \frac{k_B T^{3/2}}{\hbar T_e^{1/2}} \exp(-12T_e/T), \quad \tau_i^{-1} = 0.4c \frac{k_B}{\hbar} \frac{k_B T^{5/2}}{T_e^{3/2}},$$

where

$$T_d = \frac{(g\mu_B)^2}{k_B a^3}, \quad T_e = \frac{2SJ}{k_B}.$$

We initially re-scaled the values $T_d = 0.012$ K and $T_e = 1.0$ K employed in Ref. 36 for EuS ($T_C = 16.5$ K)

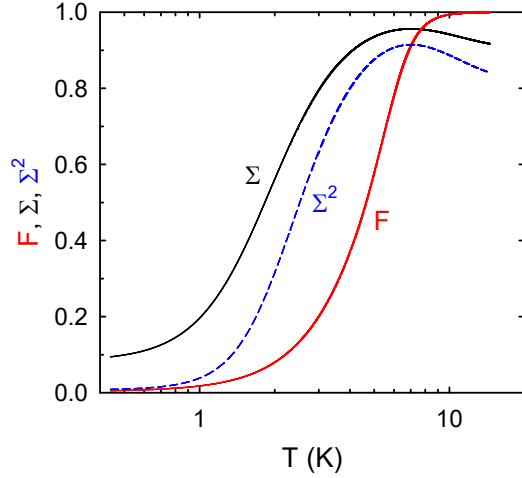


FIG. 8. Σ , Σ^2 , and $F(L_{eff})$ used for the Poiseuille analysis of κ_m^{con} for the least defective ($\ell_0 = 0.15$ mm) crystal [Fig. 3 (b)].

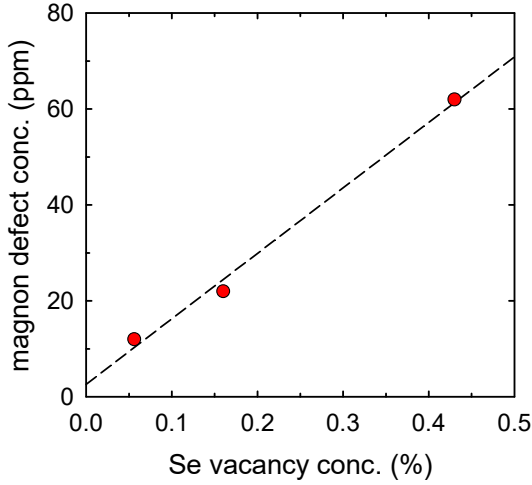


FIG. 9. Nonmagnetic defect concentration for magnons from the model fitting *vs.* Se vacancy concentration inferred from Callaway fitting of κ_L .

using the ratio of lattice constants and T_C (as a surrogate for J). These gave $T_d = 0.004$ K and $T_e = 3.5$ K. Subsequently we settled on $T_e = 4.2$ K which provided better agreement with the data for the least defective specimen. The scattering rates were adopted without modification with the exception of the exponent of the Umklapp scattering rates (we used 10 rather than 12 as above) and the prefactor of τ_{4U}^{-1} (we decreased it by a factor 380). As noted in Ref. 36, these changes put our four-magnon Umklapp scattering rate in better agreement with that computed by Schwabel and Michel [41], and produced better agreement with the data. With these modifications, the only remaining adjustable parameter was the impurity concentration (c).

The scattering rates were incorporated into an interpolation formula for the magnon thermal conductivity using the function described in Ref. 38 and derived by Alvarez and Jou [43]:

$$\kappa_m = \frac{1}{3} C_m v_m [\ell_R^B (1 - \Sigma) + \ell_R F(L_{eff}) \Sigma], \quad (F1)$$

$$F(L_{eff}) = \frac{1}{2\pi^2} \left(\frac{L_{eff}}{\ell} \right)^2 \left(\sqrt{1 + 4\pi^2 \left(\frac{\ell}{L_{eff}} \right)^2} - 1 \right),$$

where $\Sigma = 1/(1 + \ell_N/\ell_R)$, $L_{eff} = \pi\ell_0/(2\sqrt{2})$, $\ell \equiv \sqrt{\ell_N \ell_R}$, $\ell_R = (1/\ell_{3U} + 1/\ell_{4U} + 1/\ell_i)^{-1}$, and $\ell_R^B = (1/\ell_0 + 1/\ell_R)^{-1}$. We used Σ^2 in place of Σ in the above expression as it provided a better interpolation $\rightarrow 0$ at low- T (Fig. 8).

The impurity scattering concentrations (c) employed to produce the curves in Fig. 3 correlate with those found for phonon-defect scattering (Fig. 9) in the Callaway analysis of κ_L (Table I).

-
- [1] D. Douthett and S. A. Friedberg, Phys. Rev. **121**, 1662 (1961).
 - [2] D. C. Mccollum, R. L. Wild and J. Callaway, Phys. Rev. **136**, A426 (1964).
 - [3] B. Luthi, J. Phys. Chem. Solids **23**, 35 (1962).
 - [4] R. L. Douglass, Phys. Rev. **129**, 1132 (1963).
 - [5] C. M. Bhandari and G. S. Verma, Phys. Rev. **152**, 731 (1966).
 - [6] D. Walton, J. E. Rives, and Q. Khalid, Phys. Rev. B **8**, 1210 (1973).
 - [7] B. Y. Pan, T. Y. Guan, X. C. Hong, S. Y. Zhou, X. Qiu, H. Zhang, and S. Y. Li, Europhys. Lett. **103**, 37005 (2013).
 - [8] S. R. Boona and J. P. Heremans, Phys. Rev. B **90**, 064421 (2014).
 - [9] Stephen R. Boona, Roberto C. Myers and Joseph P. Heremans, Energy Environ. Sci. **7**, 885 (2014).
 - [10] A. V. Chumak, V. I. Vasyuchka, A. A. Serga, and B. Hillebrands, Nature Phys. **11**, 453 (2015).
 - [11] P. G. Meunier and M. Bertaud, J. Appl. Crystallogr. **9**, 364 (1976).
 - [12] H. Effenberger and F. Pertlik, Monatshefte für Chemie **117**, 887 (1986).
 - [13] Jan-Willem G. Bos, C. V. Colin, and T. T. M. Palstra, Phys. Rev. B **78**, 094416 (2008).
 - [14] M. Belesi, I. Rousochatzakis, H. C. Wu, H. Berger, I. V. Shvets, F. Mila, and J. P. Ansermet, Phys. Rev. B **82**, 094422 (2010).
 - [15] Judit Romhányi, Jeroen van den Brink and Ioannis Rousochatzakis, Phys. Rev. B **90**, 140404(R) (2014).

- [16] M. Ozerov, J. Romhanyi, M. Belesi, H. Berger, J.-Ph. Ansermet, Jeroen van den Brink, J. Wosnitzer, S. A. Zvyagin, and I. Rousochatzakis, *Phys. Rev. Lett.* **113**, 157205 (2014).
- [17] S. Seki, X. Z. Yu, S. Ishiwata, and Y. Tokura, *Science* **336**, 198 (2012).
- [18] T. Adams, A. Chacon, M. Wagner, A. Bauer, G. Brandl, B. Pedersen, H. Berger, P. Lemmens, and C. Pfleiderer, *Phys. Rev. Lett.* **108**, 237204 (2012).
- [19] J. Panella, B. A. Trump, G. G. Marcus, and T. M. McQueen, unpublished.
- [20] N. Prasai *et al.*, unpublished.
- [21] Y. S. Hor *et al.*, *Phys. Rev. B* **79**, 195208 (2009).
- [22] D. J. Sanders and D. Walton, *Phys. Rev. B* **15**, 1489 (1977).
- [23] S. Seki *et al.* *Phys. Rev. B* **93**, 235131 (2016).
- [24] Aitor Larrañaga, José L. Mesa, Luis Lezama, José L. Pizarro, María I. Arriortua, and Teófilo Rojo, *Mater. Res. Bull.* **44**, 1 (2009).
- [25] H. B. G. Casimir, *Physica (Amsterdam)* **5**, 495 (1938).
- [26] J. M. Ziman, *Electrons and Phonons* (Oxford University Press, Oxford, 1960).
- [27] D. Inosov, private communication.
- [28] P. Y. Portnichenko *et al.* *Nat. Commun.* **7**, 10725 (2016).
- [29] Dipole corrections to the spin-wave dispersion are negligible for $k_B T \gg \hbar\omega_m = g\mu_B 4\pi M_s$. For Cu_2OSeO_3 , $\mu_0 M_s \simeq 0.15$ T yields $\hbar\omega_m \simeq 0.018$ meV $\simeq 0.21 k_B$. Thus the quadratic dispersion should be valid for $T \gg 0.2$ K, and certainly for $T \geq 1$ K.
- [30] In the case of constant mean-free path, appropriate for the magnon-boundary scattering regime, $\kappa_m \propto T^2 \int x^3 e^x / (e^x - 1)^2 dx$, where $x = \hbar\omega/k_B T$; the integrand has a sharp maximum at $x = 2.58$. See, e.g. W. B. Yelon and L. Berger, *Phys. Rev. B* **6**, 1974 (1972).
- [31] A. Aqeel *et al.*, *Phys. Rev. B* **94**, 134418 (2016).
- [32] Suhas Gangadharaiah, A. L. Chernyshev, and Wolfram Brenig, *Phys. Rev. B* **82**, 134421 (2010).
- [33] R. N. Gurzhi, *Sov. Phys. JETP* **19**, 490 (1964).
- [34] R. A. Guyer and J. A. Krumhansl, *Phys. Rev.* **148**, 778 (1966).
- [35] A. I. Akhiezer, V. G. Bar'yakhtar, and M. I. Kaganov, *Sov. Phys. Uspekhi* **3**, 661 (1961).
- [36] J.-J. Forney and J. Jäckle, *Phys. Kondens. Materie* **16**, 147 (1973).
- [37] L. P. Mezhov-Deglin, *Sov. Phys. JETP* **22**, 47 (1966); E. M. Hogan, R. A. Guyer, and H. A. Fairbank, *Phys. Rev.* **185**, 356 (1969).
- [38] C. de Tomas, A. Cantarero, A. F. Lopeandia, and F. X. Alvarez, *J. Appl. Phys.* **115**, 164314 (2014).
- [39] R. Berman, *Thermal Conduction in Solids* (Oxford University Press, Oxford, 1976).
- [40] P. B. Allen, *Phys. Rev. B* **88**, 144302 (2013).
- [41] F. Schwabl and K. H. Michel, *Phys. Rev. B* **2**, 189 (1970).
- [42] Ratsifaritana and P. G. Klemens, *Int. J. Thermophys.* **8**, 737 (1987).
- [43] F. X. Alvarez and D. Jou, *Appl. Phys. Lett.* **90**, 083109 (2007).